Interplay between Different Magnetisms in Cr-Doped Topological Insulators

Xufeng Kou,[†] Murong Lang,[†] Yabin Fan,[†] Ying Jiang,[‡] Tianxiao Nie,[†] Jianmin Zhang,[§,⊥] Wanjun Jiang,[†] Yong Wang,[‡] Yugui Yao,[§] Liang He,[†,*] and Kang L. Wang[†,*]

[†]Department of Electrical Engineering, University of California, Los Angeles, California 90095, United States, [‡]Center for Electron Microscopy and State Key Laboratory of Silicon Materials, Department of Materials Science and Engineering, Zhejiang University, Hangzhou 310027, China, [§]School of Physics, Beijing Institute of Technology, Beijing 100081, China, and [⊥]Beijing National Laboratory for Condensed Matter Physics and Institute of Physics, Chinese Academy of Sciences, Beijing 100190, China

ABSTRACT Breaking the time-reversal-symmetry of topological insulators through magnetic doping has led to exotic physical discoveries. Here, we report the gate-dependent magneto-transport measurements on the Cr-doped $(Bi_xSb_{1-x})_2Te_3$ thin films. With effective top-gate modulations, we demonstrate the presence of both the hole-mediated RKKY coupling and carrier-independent van Vleck magnetism in the magnetic TI systems. Most importantly, by varying the Cr doping concentrations from 2% to 20%, we unveil the interplay between the two magnetic orders and establish the valid approach to either enhance or suppress each individual contribution. The electric-field-controlled ferromagnetisms identified in the Cr-doped TI materials will serve as the fundamental step to further explore the TRS-breaking TI systems, and it may also help to expand the functionality of TI-based device for spintronics applications.

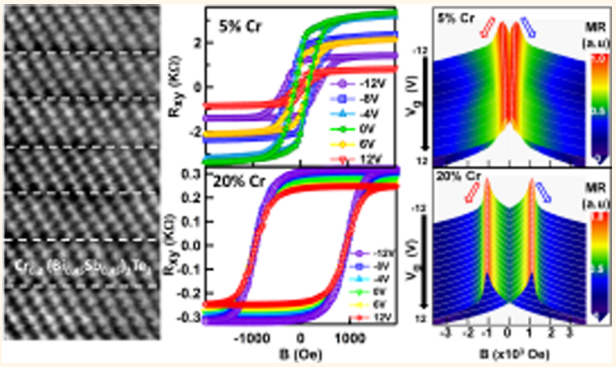

KEYWORDS: topological insulator · magnetic doping · van Vleck magnetism · electric-field-controlled ferromagnetism

The strong spin−orbit coupling and time-reversal-invariant symmetry give rise to a new class of materials known as the topological insulators (TIs).[1−7] Featured by the unique massless Dirac fermions on the boundaries, TIs are anticipated for dissipationless spin-dependent transport even at relative high temperatures. As a result, huge progress in recent years has been focused on the time-reversal-symmetry (TRS) protected TI systems.[8−11] Alternatively, if additional ferromagnetic orders are introduced, the original topologically nontrivial state will be driven into the TRS-breaking realm.[12] Associated physical phenomena like quantum anomalous Hall Effect (QAHE) and exotic particles (dyons, axions and majorana fermions) are anticipated.[13−22] All of such discoveries will further broaden the research and application scopes of topological insulators.

Introducing magnetic impurities to the surface or bulk of topological insulators has been proven to be an effective way to open a gap of the surface states.[12,23−27] To understand the magnetic origin, it has been proposed that in magnetic TI systems, ferromagnetic moments can be developed through two major mechanisms: the van Vleck mechanism and the Ruderman-Kittel-Kasuya-Yosida (RKKY) coupling.[12,14,28] In the former case, due to the large spin susceptibility of the valence electrons in the band-inverted TI materials, the magnetic ions can thus be directly coupled through these local valence electrons without the assistance of the itinerant electrons. Consequently, this "bulk ferromagnetism" is independent of the carrier density.[14] On the other hand, neighboring magnetic ions can also be coupled through the mediation of conduction carriers and this kind of coupling is referred to as the carrier-mediated RKKY interaction.[29−31] Recently, these two magnetic mechanisms were independently

* Address correspondence to heliang@ee.ucla.edu, wang@ee.ucla.edu.

Received for review July 23, 2013 and accepted September 26, 2013.

Published online September 26, 2013
10.1021/nn4038145

observed in Mn-doped $Bi_2(TeSe)_3$ and Cr-doped $(BiSb)_2Te_3$ thin films.[32,33] However, there still remains ambiguity regarding the interplay between the surface and bulk magnetizations.

In this article, we report the study of electric-field-controlled magnetisms in the Cr-doped $(Bi_xSb_{1-x})_2Te_3$ thin films. From the top-gate-modulated magneto-transport measurements, we demonstrate the presence of both the hole-mediated RKKY coupling and the carrier-independent bulk van Vleck magnetism. Significantly, we are able to separately operate on each interaction mode through the alteration of Cr doping level and electrical gating. These unique magneto-electric responses identified in the Cr-doped TI materials will serve as the fundamental step to further explore the TRS-breaking TI systems and expand the functionality of TI-based device for spintronics applications.

RESULTS AND DISCUSSION

We start the experiment with the preparation of Cr-doped $(Bi_xSb_{1-x})_2Te_3$ thin films on the insulating GaAs substrate using molecular beam epitaxy (MBE). With the surface-sensitive real-time high-energy electron diffraction (RHEED) technique, *in situ* growth dynamics is monitored.[34] Figure 1a shows the as-grown RHEED patterns taken at $t = 0$, 30, and 65 s successively. Both the sharp 2D streaky lines and the bright zero-order specular spot persist during the entire growth process, indicative of the single-crystalline feature of the sample.[35] The smooth surface morphology is later confirmed by atomic force microscopy (AFM) as shown in Figure 1b where typical TI triangular terraces are preserved without any Cr aggregations or clusters. Meanwhile, by fitting the RHEED oscillation periods in Figure 1c, the growth rate is extracted to be around 1 quintuple layer (QL)/min. More importantly, since the RHEED patterns directly reflect the in-plane atom morphology in the reciprocal k-space,[36] we can thus inspect the as-grown surface configuration by using the d-spacing evolution between the two first-order diffraction lines as shown in Figure 1a. From Figures 1c,d, it can be seen clearly that the d-spacing shrinks quickly as soon as the growth starts, and the surface transition from the pristine GaAs to the $Cr_y(Bi_xSb_{1-x})_2Te_3$ has completed immediately after the formation of the first QL. In addition, the degree of the d-spacing change (*i.e.*, −6.8%) corresponds to a Bi/Sb = 1 in the grown TI compound material.

After the sample growth, an energy dispersive X-ray (EDX) spectrometer is employed to perform elemental mappings. A thin layer of Pt is deposited during the Focused ion beam (FIB) process in order to protect the TI thin film. Figure 2a displays a typical high angle annular dark field (HAADF) image of the cross-section Cr-doped TI film from a heuristic perspective. The white contrast from the TI film clearly indicates that the $Cr_y(Bi_xSb_{1-x})_2Te_3$ film is composed of much heavier atoms compared with the GaAs substrate. Specifically, the colored EDX maps collected from both the TI (Bi, Sb, Cr, and Te) and substrate (Ga and As) are illustrated individually in Figure 2b−g. The distribution of every component (especially Cr) is uniform and there is no substitutional or interstitial doping/diffusion from the GaAs substrate, therefore leaving the bottom TI surface intact. To elaborate the detailed structural characteristics of the epitaxial film, high-resolution scanning

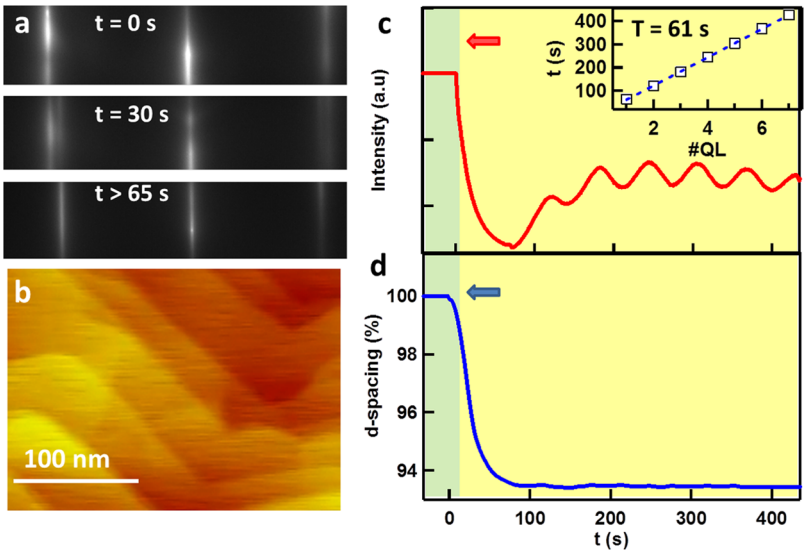

Figure 1. (a) RHEED patterns along [11$\bar{2}$0] direction of the surface of Cr-doped$(Bi_{1-x}Sb_x)_2Te_3$ thin film taken at 0, 30, and 65 s successively during growth. The surface configuration transits quickly from GaAs to TI layer. A Sharp 2D pattern with a bright specular spot can be observed during the growth. (b) AFM image of the Cr-doped TI thin film with the size of 0.3 μm × 0.3 μm. (c) RHEED oscillations of intensity of the specular beam. Inset: the growth rate of 1 QL/min is determined from the oscillation period. (d) d-spacing evolution of the surface lattice during growth. After 1 QL growth, the surface configuration from GaAs to $Cr(Bi_{1-x}Sb_x)_2Te_3$ has completed. Both arrows in (c) and (d) indicate the beginning of thin film growth.

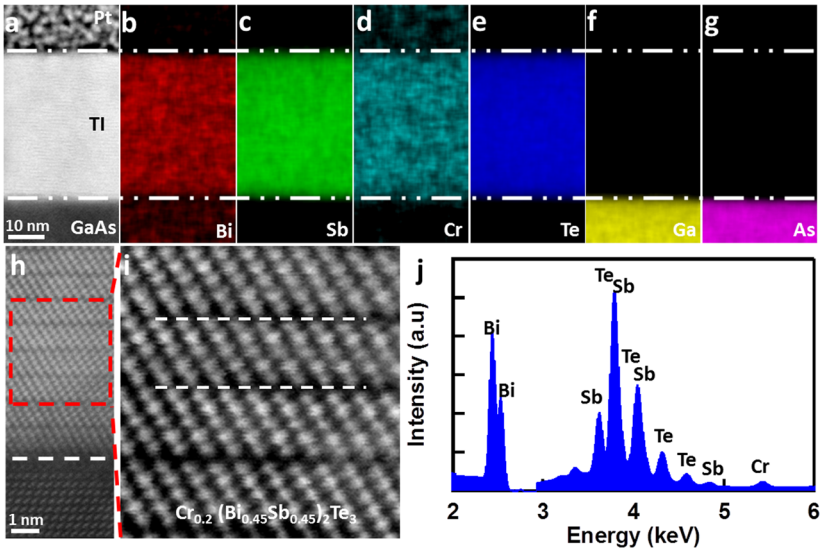

Figure 2. (a) HAADF image of the cross-section Cr-doped $(Bi_{1-x}Sb_x)_2Te_3$ film grown on the GaAs substrate. (b−g) Distribution maps of each individual element: Bi (b), Te (c), Cr(d), Ta(e), Ga(f), and As (g). Cr dopants distribute uniformly inside the TI layer. (h) High-resolution cross-sectional STEM image, showing the epitaxial single-crystalline $Cr_{0.2}(Bi_{0.45}Sb_{0.45})_2Te_3$ thin film with sharp TI−GaAs interface. (i) Zoom-in STEM to demonstrate typical quintuple-layered crystalline structure of tetradymite-type materials. Neither Cr segregations nor interstitial defects are detected. (j) EDX spectrum to examine the chemical element compositions. The Cr doping concentration is estimated to be 10%.

transmission electron microscopy (HRSTEM) investigation is performed. As shown in Figure 2h, single-crystalline $Cr_y(Bi_xSb_{1-x})_2Te_3$ film with a sharp interface can be clearly seen on top of the GaAs substrate. At the same time, the corresponding zoom-in HRTEM image in Figure 2I manifests the typical TI quintuple-layered structure. It is also identified that the van der Waals interactions between adjacent quintuple layers indeed induce a larger gap compared with the neighboring Bi/Sb−Te covalently bonded sheets. Most importantly, the highly ordered hexagonal configuration also confirms that there is no Cr interstitial defects or second phase separation inside the TI thin film. Combined with Figure 2d and the theoretical anticipations,[37] it may suggest that the Cr dopants prefer the stable substitution formation inside the host TI matrix. Furthermore, from the overall EDX spectrum in Figure 2j, the chemical composition of the Cr-TI film is calculated to be $Cr_{0.2}(Bi_{0.45}Sb_{0.45})_2Te_3$, consistent with the *d*-spacing estimation in Figure 1d. From these data, we may conclude that high-quality Cr-doped TI thin films with low defects, well-defined surfaces, and uniform Cr distribution have been prepared by MBE.

The main objective of the following study is to investigate the prevailing magnetisms in the Cr-doped TI materials. We first discuss the low-temperature magneto-transport measurements on the 6 QL $Cr_{0.04}(Bi_{0.49}Sb_{0.49})_2Te_3$ thin film with a nominal Cr doping concentration of 2%. Top-gated Hall bar devices of micrometer-scale are fabricated as shown in Figure 3a. The carrier density of this $Cr_{0.04}(Bi_{0.49}Sb_{0.49})_2Te_3$ sample is obtained to be 1.1×10^{12} cm^{-2} at 1.9 K and the Fermi level E_F without gate bias is already within the surface band gap (see Supporting Information Figure S3). As a result, the electric field provided by top gate (±12 V) can effectively tune E_F across the surface band gap (±50 meV), and therefore change the carrier type, as illustrated in Figure 3c. The gate-dependent anomalous Hall effect (AHE) is shown in Figure 3b. The total Hall resistance is expressed as $R_{xy} = R_0H + R_AM(H)$ where the ordinary Hall coefficient R_0 is inversely proportional to the Hall density, and the anomalous Hall coefficient R_A is affected by intrinsic/extrinsic scatterings.[38,39] After subtracting the linear ordinary Hall component (*i.e.*, R_0H), the nearly square-shaped hysteresis loops suggest the well-developed ferromagnetic order with the easy magnetization axis out-of-plane. More importantly, the magnetic hysteresis behavior varies dramatically when the sample is biased from *p*-type to *n*-type. Related with the ambipolar effect of the longitudinal resistance R_{xx} in Figure 3c, the change of the coercive field H_c (red hollow circles) can be divided into two distinct regions as illustrated in Figure 3d where the green and yellow parts represent the *p*-type and *n*-type regions, respectively. Particularly, when the Fermi level is below the surface band gap (-12 V $< V_g < -2$ V), H_c steadily reduces from 120 Oe down to 55 Oe, indicating a hole-mediated RKKY coupling signature (see details in Supporting Information S4). On the contrary, once the dominant conduction holes are depleted when $V_g > 0$ V, H_c slowly stops decreasing, and finally approaches to its minimum value around 40 Oe when E_F is far above the surface band gap. Similarly, the Curie temperature T_c (*i.e.*, blue solid squares in Figure 3d) which is determined from the temperature dependent R_{xy} curves (see Supporting

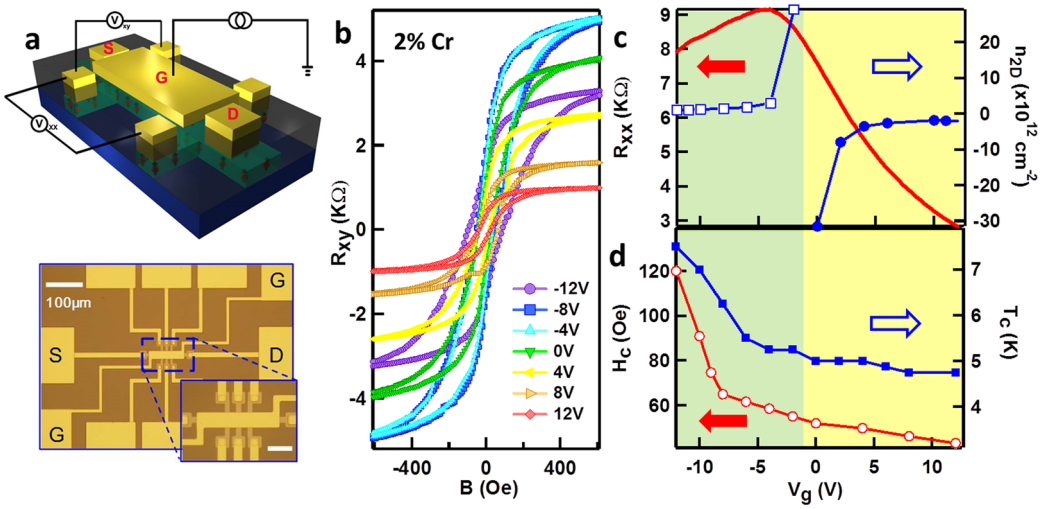

Figure 3. (a) Top-gated Hall bar device structure used for exploring the electric-field-controlled anomalous Hall effect. The effective size is 10 μm (L) × 40 μm (W). (b) Gate-dependent anomalous Hall effect at 1.9 K in 6 QL $Cr_{0.04}(Bi_{0.49}Sb_{0.49})_2Te_3$ thin films with the Cr doping levels of 2%. (c) Top-gate modulations in the 6 QL $Cr_{0.04}(Bi_{0.49}Sb_{0.49})_2Te_3$ sample. The observed ambipolar effect of R_{xx} (red solid lines) indicates that the Fermi level can be effectively tuned across the surface band gap. The Hall density (blue) determined from the linear R_{xy} curve at high field changes sign accordingly. (d) The changes of coercivity field H_c at 1.9 K (red hollow circles) and Curie temperature T_c (blue solid squares) with applied top-gate voltages. Both of them gradually decrease when the sample is biased from *p*-type to *n*-type, indicating the hole-mediated RKKY interaction signature.

Information Figure S5) also follows the reduction-and-saturation behavior by gate modulation, namely, T_c decreases from 7.5 K ($V_g = -12$ V) down to 4.7 K ($V_g > 5$ V). Given the fact that the hole-mediated RKKY interaction is completely suppressed in the region where E_F is far above the bulk valence band, both the remaining gate-independent H_c and T_c in the *n*-type region strongly support the presence of additional ferromagnetic contribution where the robust magnetic order is formed without the assistance of the itinerant carriers. We therefore may attribute the electric-field-independent magnetization to the bulk van Vleck ferromagnetism.[14,17,33] Accordingly, we may conclude that the gate-controlled AHE results in the 6 QL $Cr_{0.04}(Bi_{0.49}Sb_{0.49})_2Te_3$ sample reveal the coexistence of both hole-mediated RKKY and van Vleck mechanisms.

Our next step is to analyze the interplay between the above two magnetisms in the Cr-doped $(Bi_{0.5}Sb_{0.5})_2Te_3$ materials. By controlling the Cr doping levels during MBE growth, we have prepared additional $Cr_y(Bi_xSb_x)_2Te_3$ samples, all of which have the same Bi/Sb ratio of 1 and film thickness d = 6 QL, but different Cr doping levels. Figure 4a–d summarizes the electric-field-controlled AHE results of four samples with Cr% = 5%, 10%, 15%, and 20%, respectively. Although increasing the Cr doping concentration introduces more carriers (*i.e.*, the 2D Hall density n_{2D} varies from 1.2×10^{12} to 2.2×10^{13} cm^{-2} at 1.9 K), such defects are acceptable to maintain E_F inside the bulk band gap.[40−43] From the extracted $H_c - V_g$ curves in Figure 4e–h, we observe that in the moderate doping region (5%, 10%, and 15%), the Cr-doped $(Bi_{0.5}Sb_{0.5})_2Te_3$ thin films all exhibit the hole-mediated RKKY coupling behaviors in the sense that the anomalous Hall resistance R_{xy} loops show a quick decrease of their coercivity field (H_c) when the majority of holes are depleted. When the samples are further biased deep into the *n*-type region (*i.e* > 50 meV above the surface gap), H_c gradually saturates at finite values of 150 Oe (5%), 375 Oe (10%), and 685 Oe (15%), respectively. On the contrary, when the Cr doping concentration increases up to 20% in Figure 4d, even though the surface Fermi level has been effectively adjusted by 50 meV (inset of Figure 4h), the hysteric window (H_c) remains a constant of 1000 Oe and does not show any change with respective to the gate bias (Figure 4h).

From the detailed comparison of the AHE differences in Figure 4, we now understand the effect of Cr doping on the two magnetic origins discussed above. When the Cr concentration is smaller than 15%, the bulk van Vleck mechanism and the hole-mediation both exist in the system and contribute to the net magnetizations. With effective gate tuning, the carrier type and density can be adjusted, and the magnetic moment from the carrier-mediated RKKY exchange is therefore modulated. Given the fact that the density of states (DOS) of the Cr^{3+} ions is distributed majorly below the Dirac point, the long-range RKKY coupling in the *p*-type region thus introduces much more robust ferromagnetic moments over the weaker bulk van Vleck term; it therefore becomes the dominant component in the magnetic TI samples with moderate Cr doping. We should point out here that it is difficult to further distinguish the mediating itinerant carriers since the topological surfaces are entangled with the bulk contribution in our uniformly Cr-doped TI

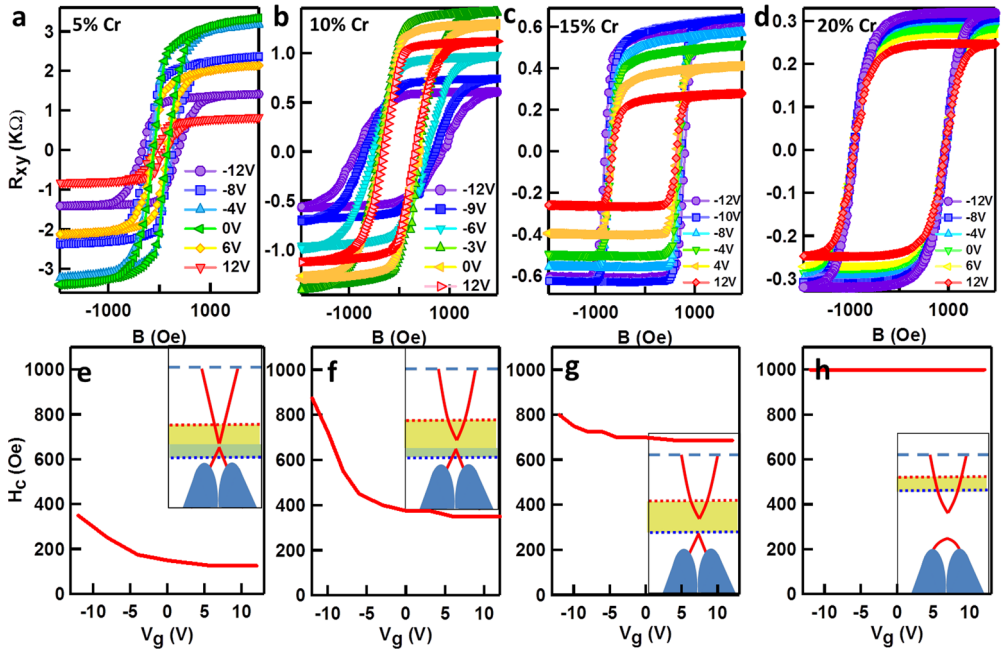

Figure 4. Gate-dependent AHE resutls for 6 QL Cr-doped $(Bi_{1-x}Sb_x)_2Te_3$ thin films with different Cr doping concentrations (a) Cr = 5%, (b) Cr = 10%, (c) Cr = 15%, and (d) Cr = 20%. (e−h) Gate-modulated coercive field changes for these four samples, respectively. Inset: Illustration of the Fermi level position as adjusted by the top-gate voltages ranging from −12 V to +12 V.

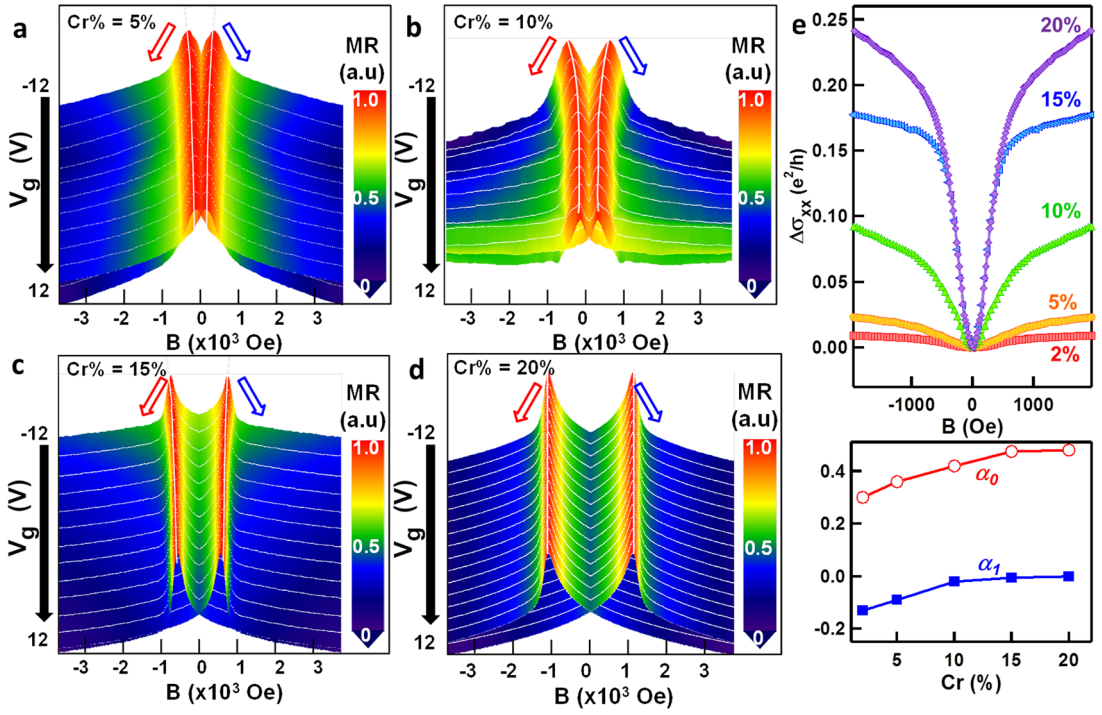

Figure 5. Gate-dependent Magneto-resistance (MR) for Cr-doped $(Bi_{1-x}Sb_x)_2Te_3$ thin films with different Cr doping concentrations (a) Cr = 5%, (b) Cr = 10%, (c) Cr = 15%, and (d) Cr = 20%. The measurements are carried out at 1.9 K with applied magnetic field out-of-plane. All of the four devices show the double-split butterfly MR curves. (e) Top: weak-localization behaviors when samples in (a) to (d) are biased in the *n*-type region where the magnetization is dominated by the bulk van Vleck term. With more Cr dopants, the positive WL cusp becomes sharper, indicating more deviation from the π-Berry phase. Bottom: WL/WAL weight factors α_0 and α_1 extracted from MC curves in (e).

samples. As more chromium atoms are incorporated in the TI system, on the one hand, the bulk van Vleck-type magnetism is expected to becomes more pronounced due to the stronger out-of-plane magnetic moments M_z from the Cr ions. On the other hand, however, since excessive Cr atoms promote the formation of *n*-type Bi_{Te} antisite defects,[37] they therefore force the Fermi level E_F "pinned" far above the surface band gap. Under

such circumstance, the hole-mediated RKKY coupling becomes diminished or even completely suppressed, leaving only the bulk van Vleck responses in heavily Cr-doped TI samples.[17,33] As a result, by designing the Cr doping profile and electric-gating strategy, we demonstrate the valid approach to either enhance or suppress the magnetic contributions from different magnetisms.

Additionally, these magneto-electric effects can also be illustrated through the magneto-resistance (MR) results. Figure 5a−d gives the electric-field-controlled three-dimensional normalized MR maps for the same samples studied in Figure 4. Like hysteresis AHE curves, the butterfly shaped double-split MR peaks are present, indicative of the remnant field generated by the ferromagnetic orders.[32] Meanwhile, the peak shifts with respect to the applied gate voltages also confirm the hole-mediated RKKY mechanism in the Cr-doped TI samples. Beside the hysteric signals shown in the MR maps, the correlated magneto-conductance (MC) curves which are defined as $\sigma_{xx} = R_{xx}/({R_{xx}}^2 + {R_{xy}}^2)$ at low magnetic field provide us additional piece of information about the Cr-doped TI conduction behaviors in the quantum diffusive region.[23,44,45] Generally speaking, the quantum interference of surface Dirac fermions depends on the Berry phase ϕ. In the magnetically doped TI systems, the formed magnetic moment M_z forces the surface states open a band gap Δ, and thus drives the Berry phase to deviate from its original π-state to $\phi = \pi(1 - \Delta/2E_F)$.[45] The corresponding weak localization (WL) behaviors are studied in Figure 5e where the MC curves of Cr-doped $(Bi_{0.5}Sb_{0.5})_2Te_3$ thin film with Cr doping concentrations ranging from 2% to 20% are presented (we deliberately shift the magnetic peaks from H_c to the zero-point for direct comparison). With the increase of Cr dopants, it can be clearly seen that the negative MC cusps at low magnetic field become sharper, indicating the larger surface gap Δ induced by the stronger magnetic order. Following the modified two components Hikami-Larkin-Nagaoka (HLN) theory that $\Delta\sigma(B) = \sum_{i=0,1}(\alpha_i e^2/\pi h)\{\psi[(l_B^2/l_{\phi i}^2) + 1/2] - \ln(l_B^2/l_{\phi i}^2)\}$ where ψ is the digamma function,[45,46] $l_B = [\hbar/(4e|B|)]^{1/2}$ is the magnetic length, and l_ϕ is the phase coherent length, we realize that the extracted WL weight factor α_0 increases from 0.3 (Cr% = 2%) to 0.48 (Cr% = 20%) and gradually approaches the ideal value of 0.5 (*i.e.*, $\Delta/2E_F = 1$ and $\phi = 0$). On the contrary, the weak antilocalization factor α_1 is almost zero in all the $Cr_y(Bi_xSb_x)_2Te_3$ samples. Accordingly, the systematic changes of the MC phenomena observed in Figure 5e are consistent with the AHE results, again verifying the correlation between the robust magnetizms in the Cr-doped TI thin films.

CONCLUSIONS

In summary, we demonstrate the realization of gate-independent van Vleck magnetism and carrier-mediated RKKY interaction in Cr-doped $(Bi_xSb_{1-x})_2Te_3$ systems. The understanding of the interplay between these two mechanisms may provide a suitable platform to further studies of exotic TRS-breaking topological physics. Additionally, the manipulation of electric-field-controlled magnetism through varied magnetic doping may also facilitate the extension of TIs to practical low-power-dissipation electronics and spintronics applications.

EXPERIMENTAL METHODS

MBE Growth. Thin-film growth was performed using an ultrahigh vacuum Perkin-Elmer MBE system. Semi-insulating ($\rho > 10^6$ Ω·cm) GaAs (111) substrates were preannealed in the growth chamber at up to 580 °C to remove the native oxide. High-purity Bi (99.9999%), Te (99.9999%), Cr (99.99%) and Sb (99.999%) were evaporated by conventional effusion cells and cracker cells. During the growth, the GaAs (111) substrate was maintained at 200 °C (growth temperature). Epitaxial growth was monitored by an *in situ* RHEED technique, and digital images of the RHEED were captured using a KSA400 system built by K-space Associates, Inc.

Characterizations. *HRSTEM.* High-resolution STEM experiments were performed on a FEI TITAN Cs-corrected STEM operating at 200 KV and the HAADF images were acquired using a Fischione HAADF detector.

Magneto-Transport Measurements. Four-point Hall measurements were conducted using the Quantum Design physical property measurement system (PPMS). We are able to systematically alter several experimental variables such as temperature, magnetic field, measurement frequency, and external gate bias. Multiple lock-in-amplifiers and Keithley source meters were also connected with the PPMS system, enabling compressive and high-sensitivity transport measurements for the top-gated Hall bar and capacitor devices.

Device Fabrication. The Cr-doped $(Bi_{0.5}Sb_{0.5})_2Te_3$ thin films were patterned into a micrometer-scale Hall bar geometry using conventional optical photolithography with subsequent CHF_3 dry etching of 18 s. A 20 nm thick high-κ Al_2O_3 dielectric layer was deposited by atomic layer deposition (ALD) at 250 °C. Hall channel contacts were defined by *e*-beam evaporation after Al_2O_3 was etched away in the contact areas. A metal stack of Ti/Al (20 nm/100 nm) was directly deposited onto the exposed TI top surface. A top-gate metal scheme of Ti/Au (10 nm/90 nm) was achieved by the second step of photolithography and *e*-beam evaporation.

Conflict of Interest: The authors declare no competing financial interest.

Acknowledgment. The authors would like to thank the support from Focus Center Research Program-Center on Functional Engineered Nano Architectonics (FENA) and Defense Advanced Research Projects Agency (DARPA) with grants N66001-12-1-4034 and N66001-11-1-4105. K.L.W. also acknowledges the support of the Raytheon endowed chair professorship. Y.W. acknowledges support from Natural Science Foundation of China (11174244) and Zhejiang Provincial Natural Science Foundation of China (LR12A04002) and National Young 1000 Talents Plan. Y.Y. was supported by National Basic Research Program of China (973 Program Grants No. 2011CBA00100), National Natural Science Foundation of China (Grants No. 10974231 and 11174337).

Supporting Information Available: Magnetic property characterizations with SQUID, determination of the carrier density

from AHE effects, Hall resistance under high magnetic field, temperature-dependent AHE effects in Cr-doped $(Bi_xSb_{1-x})_2Te_3$ samples, hole-mediated RKKY interaction in Cr-doped $(Bi_xSb_{1-x})_2Te_3$ system, temperature-dependent AHE effects in Cr-doped $(Bi_xSb_{1-x})_2Te_3$ samples, and quantum interference in undoped $(Bi_{0.5}Sb_{0.5})_2Te_3$ thin films. This material is available free of charge *via* the Internet at http://pubs.acs.org.

REFERENCES AND NOTES

1. Kane, C. L.; Mele, E. J. Z(2) Topological Order and the Quantum Spin Hall Effect. *Phys. Rev. Lett.* **2005**, *95*, 146802.
2. Kane, C. L.; Mele, E. J. Quantum Spin Hall Effect in Graphene. *Phys. Rev. Lett.* **2005**, *95*, 226801.
3. Bernevig, B. A.; Hughes, T. L.; Zhang, S. C. Quantum Spin Hall Effect and Topological Phase Transition in HgTe Quantum Wells. *Science* **2006**, *314*, 1757–1761.
4. Moore, J. E.; Balents, L. Topological Invariants of Time-Reversal-Invariant Band Structures. *Phys Rev B* **2007**, *75*, 121306.
5. Fu, L.; Kane, C. L.; Mele, E. J. Topological Insulators in Three Dimensions. *Phys. Rev. Lett.* **2007**, *98*, 106803.
6. Jiang, Y. P.; Wang, Y. L.; Chen, M.; Li, Z.; Song, C. L.; He, K.; Wang, L. L.; Chen, X.; Ma, X. C.; Xue, Q. K. Landau Quantization and the Thickness Limit of Topological Insulator Thin Films of Sb_2Te_3. *Phys. Rev. Lett.* **2012**, *108*, 016401.
7. Xu, S. Y.; Xia, Y.; Wray, L. A.; Jia, S.; Meier, F.; Dil, J. H.; Osterwalder, J.; Slomski, B.; Bansil, A.; Lin, H.; *et al.* Topological Phase Transition and Texture Inversion in a Tunable Topological Insulator. *Science* **2011**, *332*, 560–564.
8. Konig, M.; Wiedmann, S.; Brune, C.; Roth, A.; Buhmann, H.; Molenkamp, L. W.; Qi, X. L.; Zhang, S. C. Quantum Spin Hall Insulator State in HgTe Quantum Wells. *Science* **2007**, *318*, 766–770.
9. Hsieh, D.; Qian, D.; Wray, L.; Xia, Y.; Hor, Y. S.; Cava, R. J.; Hasan, M. Z. A Topological Dirac Insulator in a Quantum Spin Hall Phase. *Nature* **2008**, *452*, 970–U975.
10. Qi, X. L.; Zhang, S. C. The Quantum Spin Hall Effect and Topological Insulators. *Phys. Today* **2010**, *63*, 33–38.
11. Zhang, Y.; He, K.; Chang, C. Z.; Song, C. L.; Wang, L. L.; Chen, X.; Jia, J. F.; Fang, Z.; Dai, X.; Shan, W. Y.; *et al.* Crossover of the Three-Dimensional Topological Insulator Bi_2Se_3 to the Two-Dimensional Limit. *Nat. Phys.* **2010**, *6*, 584–588.
12. Liu, Q.; Liu, C. X.; Xu, C. K.; Qi, X. L.; Zhang, S. C. Magnetic Impurities on the Surface of a Topological Insulator. *Phys. Rev. Lett.* **2009**, *102*, 156603.
13. Liu, C. X.; Qi, X. L.; Dai, X.; Fang, Z.; Zhang, S. C. Quantum Anomalous Hall Effect in $Hg_{1-y}Mn_yTe$ Quantum Wells. *Phys. Rev. Lett.* **2008**, *101*, 146802.
14. Yu, R.; Zhang, W.; Zhang, H. J.; Zhang, S. C.; Dai, X.; Fang, Z. Quantized Anomalous Hall Effect in Magnetic Topological Insulators. *Science* **2010**, *329*, 61–64.
15. Jiang, H.; Qiao, Z. H.; Liu, H. W.; Niu, Q. Quantum Anomalous Hall Effect with Tunable Chern Number in Magnetic Topological Insulator Film. *Phys. Rev. B* **2012**, *85*, 045445.
16. Qi, X. L. Generic Wave-Function Description of Fractional Quantum Anomalous Hall States and Fractional Topological Insulators. *Phys. Rev. Lett.* **2011**, *107*, 126803.
17. Chang, C. Z.; Zhang, J.; Feng, X.; Shen, J.; Zhang, Z.; Guo, M.; Li, K.; Ou, Y.; Wei, P.; Wang, L. L.; *et al.* Experimental Observation of the Quantum Anomalous Hall Effect in a Magnetic Topological Insulator. *Science* **2013**, *340*, 167–170.
18. Li, R. D.; Wang, J.; Qi, X. L.; Zhang, S. C. Dynamical Axion Field in Topological Magnetic Insulators. *Nat. Phys.* **2010**, *6*, 284–288.
19. Moore, J. E. The Birth of Topological Insulators. *Nature* **2010**, *464*, 194–198.
20. Moore, J. Topological Insulators the Next Generation. *Nat. Phys.* **2009**, *5*, 378–380.
21. Fu, L.; Kane, C. L. Probing Neutral Majorana Fermion Edge Modes with Charge Transport. *Phys. Rev. Lett.* **2009**, *102*, 216403.
22. Akhmerov, A. R.; Nilsson, J.; Beenakker, C. W. J. Electrically Detected Interferometry of Majorana Fermions in a Topological Insulator. *Phys. Rev. Lett.* **2009**, *102*, 216404.
23. Liu, M. H.; Zhang, J. S.; Chang, C. Z.; Zhang, Z. C.; Feng, X.; Li, K.; He, K.; Wang, L. L.; Chen, X.; Dai, X.; *et al.* Crossover between Weak Antilocalization and Weak Localization in a Magnetically Doped Topological Insulator. *Phys. Rev. Lett.* **2012**, *108*, 036805.
24. Chen, Y. L.; Chu, J. H.; Analytis, J. G.; Liu, Z. K.; Igarashi, K.; Kuo, H. H.; Qi, X. L.; Mo, S. K.; Moore, R. G.; Lu, D. H.; *et al.* Massive Dirac Fermion on the Surface of a Magnetically Doped Topological Insulator. *Science* **2010**, *329*, 659–662.
25. Xu, S. Y.; Neupane, M.; Liu, C.; Zhang, D. M.; Richardella, A.; Wray, L.; Alidoust, N.; Leandersson, M.; Balasubramanian, T.; Barriga, J.; *et al.* Hedgehog Spin Texture and Berry's Phase Tuning in a Magnetic Topological Insulator. *Nat. Phys.* **2012**, *8*, 616–622.
26. Wray, L. A.; Xu, S. Y.; Xia, Y. Q.; Hsieh, D.; Fedorov, A. V.; Hor, Y. S.; Cava, R. J.; Bansil, A.; Lin, H.; Hasan, M. Z. A Topological Insulator Surface under Strong Coulomb, Magnetic and Disorder perturbations. *Nat. Phys.* **2011**, *7*, 32–37.
27. Abanin, D. A.; Pesin, D. A. Ordering of Magnetic Impurities and Tunable Electronic Properties of Topological Insulators. *Phys. Rev. Lett.* **2011**, *106*, 136802.
28. Zhu, J. J.; Yao, D. X.; Zhang, S. C.; Chang, K. Electrically Controllable Surface Magnetism on the Surface of Topological Insulators. *Phys. Rev. Lett.* **2011**, *106*, 097201.
29. Ruderman, M. A.; Kittel, C. Indirect Exchange Coupling of Nuclear Magnetic Moments by Conduction Electrons. *Phys. Rev.* **1954**, *96*, 99–102.
30. Yosida, K. Magnetic Properties of Cu-Mn Alloys. *Phys. Rev.* **1957**, *106*, 893–898.
31. Jungwirth, T.; Sinova, J.; Masek, J.; Kucera, J.; MacDonald, A. H. Theory of Ferromagnetic (III,Mn)V Semiconductors. *Rev. Mod. Phys.* **2006**, *78*, 809–864.
32. Checkelsky, J. G.; Ye, J. T.; Onose, Y.; Iwasa, Y.; Tokura, Y. Dirac-Fermion-Mediated Ferromagnetism in a Topological Insulator. *Nat Phys* **2012**, *8*, 729–733.
33. Chang, C.-Z.; Zhang, J.; Liu, M.; Zhang, Z.; Feng, X.; Li, K.; Wang, L.-L.; Chen, X.; Dai, X.; Fang, Z.; *et al.* Thin Films of Magnetically Doped Topological Insulator with Carrier-Independent Long-Range Ferromagnetic Order. *Adv. Mater.* **2013**, *25*, 1065–1070.
34. Lehmpfuhl, G.; Ichimiya, A.; Nakahara, H. Interpretation of RHEED Oscillations During MBE Growth. *Surf. Sci.* **1991**, *245*, L159–L162.
35. Kou, X. F.; He, L.; Xiu, F. X.; Lang, M. R.; Liao, Z. M.; Wang, Y.; Fedorov, A. V.; Yu, X. X.; Tang, J. S.; Huang, G.; *et al.* Epitaxial Growth of High Mobility Bi_2Se_3 Thin Films on CdS. *Appl. Phys. Lett.* **2011**, *98*, 242102.
36. Morishita, Y.; Goto, S.; Nomura, Y.; Tamura, M.; Isu, T.; Katayama, Y. Real-Time Scanning Microprobe Reflection High-Energy Electron-Diffraction Observations of Ingaas Surfaces during Molecular-Beam Epitaxy on Inp Substrates. *J. Vac. Sci. Technol., B* **1994**, *12*, 2532–2540.
37. Zhang, J. M.; Zhu, W. G.; Zhang, Y.; Xiao, D.; Yao, Y. G. Tailoring Magnetic Doping in the Topological Insulator Bi_2Se_3. *Phys. Rev. Lett.* **2012**, *109*, 266405.
38. Berger, L. Side-Jump Mechanism for the Hall Effect of Ferromagnets. *Phys. Rev. B: Solid State* **1970**, *2*, 4559–4566.
39. Fert, A. Skew Scattering in Alloys with Cerium Impurities. *J. Phys. F: Met. Phys.* **1973**, *3*, 2126–2142.
40. He, L.; Xiu, F. X.; Yu, X. X.; Teague, M.; Jiang, W. J.; Fan, Y. B.; Kou, X. F.; Lang, M. R.; Wang, Y.; Huang, G.; *et al.* Surface-Dominated Conduction in a 6 nm thick Bi_2Se_3 Thin Film. *Nano Lett.* **2012**, *12*, 1486–1490.
41. Analytis, J. G.; McDonald, R. D.; Riggs, S. C.; Chu, J. H.; Boebinger, G. S.; Fisher, I. R. Two-Dimensional Surface State in the Quantum Limit of a Topological Insulator. *Nat. Phys.* **2010**, *6*, 960–964.
42. Arakane, T.; Sato, T.; Souma, S.; Kosaka, K.; Nakayama, K.; Komatsu, M.; Takahashi, T.; Ren, Z.; Segawa, K.; Ando, Y. Tunable Dirac Cone in the Topological Insulator $Bi_{2-x}Sb_xTe_{3-y}Se_y$. *Nat. Commun.* **2012**, *3*, 636.
43. Hong, S. S.; Cha, J. J.; Kong, D. S.; Cui, Y. Ultra-low Carrier Concentration and Surface-Dominant Transport in Antimony-Doped Bi_2Se_3 Topological Insulator Nanoribbons. *Nat. Commun.* **2012**, *3*, 757.

44. Lang, M. R.; He, L.; Kou, X. F.; Upadhyaya, P.; Fan, Y. B.; Chu, H.; Jiang, Y.; Bardarson, J. H.; Jiang, W. J.; Choi, E. S.; *et al.* Competing Weak Localization and Weak Antilocalization in Ultrathin Topological Insulators. *Nano Lett.* **2013**, *13*, 48–53.
45. Lu, H. Z.; Shi, J. R.; Shen, S. Q. Competition between Weak Localization and Antilocalization in Topological Surface States. *Phys. Rev. Lett.* **2011**, *107*, 076801.
46. Lu, H. Z.; Shen, S. Q. Weak Localization of Bulk Channels in Topological Insulator Thin Films. *Phys. Rev. B* **2011**, *84*, 125138.